EDGE ARTICLE

Check for updates

Three-dimensional covalent organic framework-based artificial interphase layer endows lithium metal anodes with high stability†

Kaiyang Zheng,[a] Zhengyang Gou,[a] Cen Zhang,[a] Yuqiang Zhang,[a] Yaying Dou,[bc] Shaojie Liu, [ID] *[a] Yongheng Zhang[d] and Yantao Zhang [ID] *[a]

To gain a deeper understanding and address the scientific challenges of lithium dendrite growth, a robust solid-state electrolyte interface (SEI) with good mechanical properties and rapid ion conduction is crucial for the advancement of lithium metal batteries. Artificial SEI layers based on organic polymers, such as covalent organic frameworks (COF), have garnered widespread attention due to their flexible structural design and tunable functionality. In this work, a COF with 3D spatial geometric symmetry and a fully covalent *dia* topology was synthesized and used as artificial SEI layers. A combination of comprehensive DFT calculations and *ex situ/in situ* characterizations have unraveled the impact of interpenetrated chain segments and anchoring lithiophilic groups on the microscopic dynamics related to Li ion desolvation, charge transfer, migration pathways, and deposition morphology. The ultralow polarization voltage of 46 mV for 9400 hours with a symmetric Li|Li cell at a harsh current density of 10 mA cm^{-2}, as well as the high Li$^+$ utilization, low polarization voltage, and prolonged lifespan for 3D-COF-modified Li|S and Li|LFP full cells, unambiguously corroborate the interphase reliability. This work also aims to shed new light on the use of multi-dimensional porous polymer SEI layers to revive highly stable Li metal batteries.

Introduction

Commercial lithium-ion batteries (LIBs) are reaching their energy ceiling, and it is difficult to exceed a cruising range of more than 500 km in the field of four-wheeled electric vehicles.[1,2] A pivotal shift in the landscape of rechargeable high-energy density batteries beyond state-of-the-art LIBs has paved the way for growing demand for high-energy storage devices.[3–5] Both academia and industry are exploring alternative rechargeable batteries using advanced electrode materials paired with sulfur, oxygen, *etc.*[6–11] Lithium metal has emerged as one of the most promising alternatives and is poised to perfectly balance the ambitious targets, due to its extremely high theoretical capacity (3860 mA h g^{-1}), as well as the lowest negative electrochemical potential (−3.040 V *vs.* SHE).[12,13]

However, in order to reinvigorate Li metal anodes (LMAs), the adverse effects of high reactivity on the electrolyte interface must be avoided.[14–18] (i) The irreversible parasitic reactions between the reactive Li anode and electrolytes reduces the effective Li content and reduces the utilization of lithium metal batteries. (ii) The spontaneous solid electrolyte interface (SEI) layer struggles to suppress the corrosion of metallic Li after suffering from repeated rupture and disintegration. (iii) Li$^+$ tends to be unevenly concentrated and deposited in hotspots, and the SEI breaks during the charge and discharge processes in liquid electrolytes, resulting in unrestricted growth of lithium dendrites and isolation of dead Li. As a consequence, the practical application of lithium metal batteries (LMBs), such as Li–LiFePO$_4$, Li–S, Li–O$_2$, *etc.*, is seriously hindered owing to their inferior coulombic efficiencies, fatal safety issues, and shrinking lifespan, triggered by the notorious lithium dendrite growth and fragile SEI.[19–22]

Considerable efforts have been devoted to solving these obstacles of LMBs, including the use of three-dimensional collectors, solid-state electrolytes, and artificial solid-state electrolyte interfacial layers.[23–27] Among them, constructing a robust interfacial layer to regulate the transfer and distribution of charge/solvent molecules has emerged as one of the most versatile strategies.[28–31] Recently, micro/nanoporous interfacial pre-modification has been viably deployed to modulate the plating/stripping behaviours and pathways of Li$^+$ transportation due to their unique specific surface, pore size

[a]College of Chemistry and Pharmaceutical Engineering, Hebei University of Science and Technology, Shijiazhuang, 050018, China. E-mail: sjliu16@163.com; ytzhang@hebust.edu.cn

[b]Interdisciplinary Research Center for Sustainable Energy Science and Engineering (IRC4SE^2), School of Chemical Engineering, Zhengzhou University, Zhengzhou 450001, China

[c]Key Laboratory of Advanced Energy Materials Chemistry (Ministry of Education), College of Chemistry, Nankai University, Tianjin 300071, China

[d]Risun New Energy Technology Co., Ltd., Beijing 100070, China

† Electronic supplementary information (ESI) available. See DOI: https://doi.org/10.1039/d4sc05297h

and interconnected structure.[32–35] The fabrication of an interfacial pre-modification layer on LMAs mainly involves the following examples: metal oxides (such as TiO_2, Al_2O_3),[36–38] carbon materials (graphene, composite carbon nanotubes),[39–41] and organic polymers (polymer films).[42–45] Compared with inorganic materials, electrically insulating polymer matrixes with tunable functional groups and satisfactory structural flexibility have been shown to greatly expedite Li^+ diffusion and alleviate the proliferation of Li dendrites.[21,33,46]

Covalent organic frameworks (COF) are regarded as an emerging class of porous crystalline organic polymers, crafted from multivalent monomers linked by covalent bonds.[47–49] Their attractive periodic network structure, functional skeleton, adjustable pore size, and large surface area provide a multifaceted platform for artificial solid-electrolyte interphase layers to tailor Li^+ diffusion and transfer. Chen *et al.* developed a TpPa-COF with regularly arranged lithophilic sites (O, N) with a low surface work function to enable homogeneous lithium deposition/dissolution.[50] Guo's group reported a highly selective Li^+ transfer pathway *via* a specific cation-oriented channel using an ingenious nitro-functionalized COF artificial solid-electrolyte interface.[51] This efficient strategy has also been consolidated by our previous work incorporating versatile functionalities into layered and overlapping-stack structures of two-dimensional (2D) COFs, such as a highly crystalline spherical S–COF,[34] a self-exfoliated TpTG-COF nano-mesh,[35] and a TFSI⁻-grafted anionic COF.[52]

Three-dimensional (3D) materials have attracted attention due to their excellent structural stability, high porosity, and easily controllable spatial structure. In sharp contrast with the restricted eclipsed mode in 2D sheets, the analogous three-dimensional (3D) COFs are fully interconnected covalent systems with building blocks unfolded into three-dimensional space providing a large number of contiguous pores, which greatly improves the channel utilization, and effectively slows down the volume expansion and Li dendritic crystal growth in spatially confined structures.[53–55] In addition, the number of unburied and expanded lithophilic sites can accelerate Li^+ accommodation in the interfacial electric double layer. In terms of the striking topology diagrams of 3D COF, it is anticipated to dissect the intrinsically mechanistic understandings of multifold interpenetrated nets modulating interfacial Li^+ migration and transfer behaviors.

In light of this, a highly crystalline 3D TAM-Dha-COF (TD-COF) fabricated with a seven-fold interpenetrated diamond (*dia-c7*) topology was synthesized and utilized as an artificial SEI layer to regulate the deposition of lithium, as illustrated in Scheme 1. The large number of lithiophilic linkage sites of –C═N– and –OH spread throughout the fully conjugated backbone not only dilute the local concentration gradient of Li^+ flux passing through the multidimensional nanochannels, but also expedite the uniform Li plating in each direction. The TD-COF-dominated lithium-ion transfer energy barriers were calculated, and the conceivable Li^+ migration channels were also profiled. The original mechanisms of macroscopic electrochemical behaviours on Li metal interfacial stability are in accord with the Li^+ high-speed diffusion throughout the unstacked 3D COF transport channels and multi-directional pore architecture. Compared with pristine Li, the resulting TD-COF@Li electrode demonstrates excellent reversibility of elevated Li^+ utilization, slight polarization, and prolonged cyclic performance in Li|Cu, Li|Li, and Li-based full cells operated at harsh current densities. This compelling evidence proves that the TD-COF artificial SEI layer showcases tremendous potential for accelerated uniform transfer of Li^+ and lithium dendrite suppression.

Results and discussion

The proposed three-dimensional TD-COF was synthesized *via* a Schiff base reaction between tetrahedral 4-[tris(4-aminophenyl)methyl]aniline (TAPM) and linear 2,5-dihydroxyterephthalaldehyde (DHBA) monomers, as depicted in Scheme 1 and Fig. S1.† Subsequently, the inherent chemical components, structure and morphology features of the obtained TD-COF were defined by a variety of characterizations. As shown in Fig. 1a, the combination of the disappearance of the characteristic –NH_2 peak (3394 cm⁻¹) of TAPM and the characteristic –C═O peak (1661 cm⁻¹) of DHBA with the appearance of an imine bond (C═N) stretching vibration peak at 1611 cm⁻¹ in TD-COF provides compelling evidence for a high degree of condensation.[52] Meanwhile, additional confirmation of polymerization was shown by C═N bond formation, supported by the characteristic peak at 1550 cm⁻¹ in the Raman spectrum (Fig. 1b) and by the intense signal at 163 ppm in the ¹³C solid-state NMR (Fig. 1c).

The geometric crystallinity and unit cell parameters of TD-COF were deciphered using powder X-ray diffraction (XRD) patterns and a spatial structure simulation, as shown in Fig. 1d and S2.† The spatial model of TD-COF was assessed on the basic of a seven-fold interpenetrated *dia* topology until the geometric energy is minimized. The simulated parameters of the unit cell were $\alpha = \beta = \gamma = 90°$, $a = b = 19.81$ Å, and $c = 9.08$ Å, in line with the determined space group of $I4_1/a$ (Table S1†). As anticipated, the XRD curve was in precise agreement with the Pawley refinement theoretical pattern, in which the prominent diffraction peaks that appeared at 8.82, 10.98, 17.68 and 24.46° are assigned to the (200), (101), (400) and (501) crystal planes, respectively.[56] Scanning electron microscopy (SEM) and high-resolution transmission electron microscopy (HRTEM) were also performed to observe the microscopic structure of TD-COF. The TD-COF clearly displays an octahedral aggregated geometry with a particle size of about 200 nm, as shown in Fig. 1e, S3 and S4,† which is closely related to the dimensional transformation.[57] Meanwhile, the clear lattice fringes with an interplanar distance of 1.01 nm in Fig. 1f are in accordance with the (200) lattice plane in the XRD patterns. Accordingly, the energy dispersive spectrum (EDS) indicates evenly distributed C, N, and O elements on the excellent crystalline TD-COF (Fig. S5†). The N_2 adsorption/desorption isotherms of TD-COF were measured at 77 K, as shown in Fig. S6.† The Brunauer–Emmett–Teller (BET) specific surface area of TD-COF was calculated to be 279.2287 m² g⁻¹. The pore size distribution of TD-COF was mainly centralized at 0.8 nm based on the non-local density functional theory (NL-DFT), and the corresponding pore volume
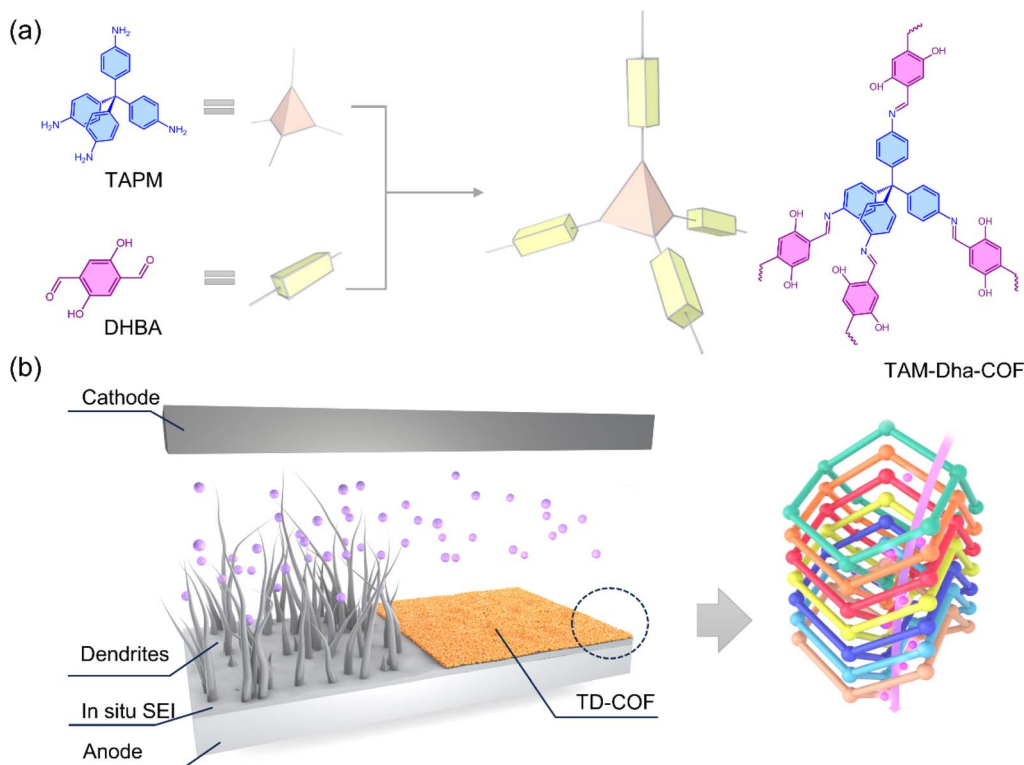
Scheme 1 (a) The synthesis of TD-COF derived from TAPM and DHBA monomers, and (b) lithium deposition and growth with and without TD-COF modification *via* a 3D spatial configuration.
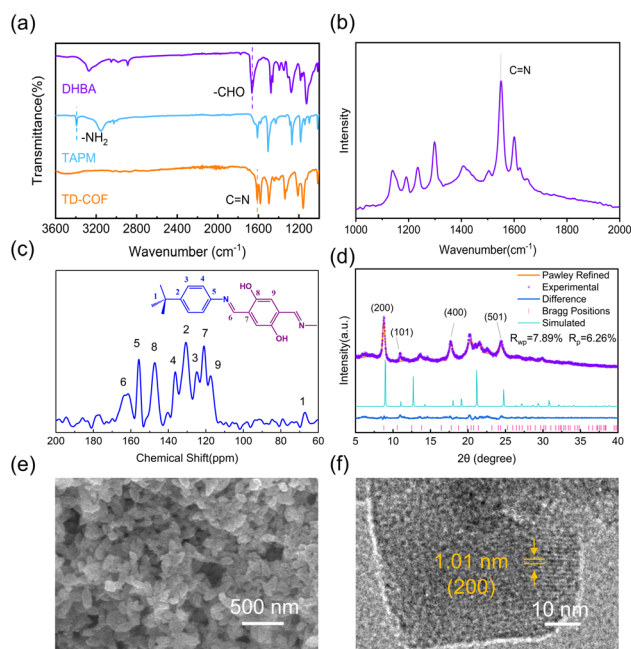

Fig. 1 Structure and surface morphology of the targeted TD-COF. (a) FT-IR spectra, (b) Raman spectrum, (c) ^{13}C solid-state NMR spectrum, (d) XRD patterns and the corresponding Pawley refinements, (e) SEM image and (f) HRTEM image of the synthesized TD-COF.

is 0.379 cm^3 g^{-1}. The above-mentioned evidence indicates that the highly crystalline *dia-c7* model TD-COF is critically contingent on the flexible junction with tetrahedral and linear linkers.

Comparative density functional theory (DFT) calculations were employed to dissect the interaction mechanisms between lithium bis(trifluoromethanesulfonyl)imide (LiTFSI) and TD-COF fragments and solvents (DME and DOL). The optimized geometric conformations (Fig. 2a) show that Li$^+$ and LiTFSI exhibit lower binding energies of −1.44 eV and −1.69 eV with the immobilized electronegative oxygen and nitrogen atoms (Fig. 2b) anchored in the TD-COF skeleton, which are significantly lower than those of Li$^+$ with DME (−0.76 eV), DOL (−0.90 eV) and TFSI$^-$ (−1.10 eV). The results show that the energetic Li$^+$ interactions with TD-COF can facilitate the Li$^+$ desolvation from the solvent cluster and expedite the adsorption on the nitrogen and oxygen sites of TD-COF. The final TFSI$^-$ anion readily couples to the Li$^+$-enriched TD-COF interfacial layer, as evidenced by the much lower binding energy of −1.69 eV, which leads to an enhanced local concentration of LiTFSI electrolyte. The chemical affinity of Li$^+$ in TD-COF impregnated with LiTFSI electrolyte was further verified using ^{7}Li solid-state nuclear magnetic resonance (ssNMR) experiments. The significant chemical shift of the LiTFSI@TD-COF sample from −1.14 ppm to −0.28 ppm in Fig. 2c is attributed to the deshielding effect of the electron-withdrawing groups –OH and –C═N– in TD-COF.[58] Based on the aforementioned DFT calculations, it can be concluded that the numerous dispersed –OH and –C═N– functional groups and versatile three-dimensional geometry framework of TD-COF unambiguously accelerate the Li$^+$ transfer kinetics to mitigate the Li$^+$ concentration gradient variation.

The implementability and influence of the TD-COF interface layer on reversible Li deposition and dissolution was assessed
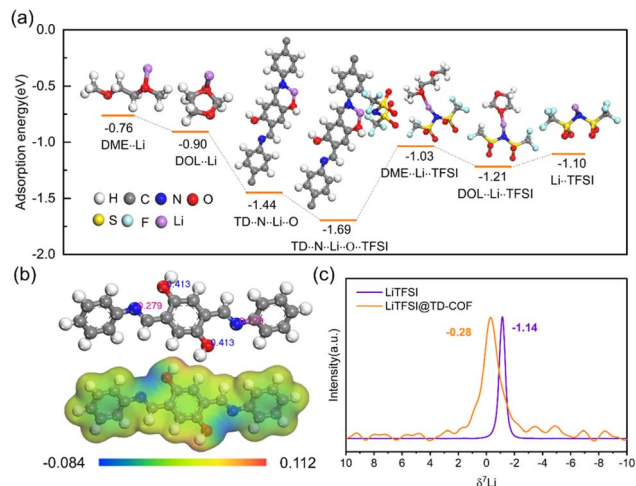
Fig. 2 Molecular coordination environment between 3D-COF fragments and LiTFSI-based electrolyte. (a) Simulated adsorption energy of LiTFSI with different solvent types and 3D-COF fragments. (b) Mulliken population analysis and electrostatic potential distribution map. (c) ^{7}Li solid-state NMR spectra.

Fig. 3 The comprehensive electrochemical reversibility of a Li metal anode with and without a TD-COF coating layer in 1 M LiTFSI DOL/DME with 2 wt% LiNO$_3$ as electrolyte. Coulombic efficiency (a) and nucleation overpotential (b) of asymmetric Li|Cu batteries at 0.5 mA cm^{-2} and 1 mA h cm^{-2}. The galvanostatic cycling profiles (c and d) and rate performance (e) of Li|Li symmetric batteries at various plating current densities and capacities.

via systematic electrochemical measurements. The modified electrodes were fabricated by drop-casting a TD-COF suspension onto copper foil and lithium foil, respectively. Asymmetrical Li|Cu cells were assembled with TD-COF@Cu and bare Cu as the working electrodes. The lithium nucleation overpotential is an important descriptor that was used to scrutinize the lithophilicity and mass transfer barrier. As shown in Fig. 3a, the TD-COF@Cu electrode garners a much lower nucleation overpotential of 47.3 mV than that of 122.0 mV for bare Cu, revealing a dynamic downhill Li nucleation barrier for the TD-COF@Li-based cell. In addition to the initial higher overpotential of TD-COF (125.0 mV) compared to bare Cu (64.6 mV) during pre-activation shown in Fig. S7,† the voltage hysteresis decreased to 34.3 mV at the 60th cycle, and 31.3 mV at the 120th cycle, and these values are lower than those obtained for the bare Cu foil of 38.2 mV and 68.6 mV. From the combination of the lower nucleation barrier and the accordant DFT calculations, it can be concluded that numerous lithophilic sites (N and O atoms) and the well-defined spatial channels play crucial roles in accelerating the mass transfer dynamics. Compared with the significantly decreased coulombic efficiency (CE) after 90 cycles found for bare Cu cells, the TD-COF@Cu anode was tested for a prolonged run of 140 cycles and retained a coulombic efficiency of 95.05% at 0.5 mA cm^{-2} with a fixed capacity of 1 mA h cm^{-2}, as shown in Fig. 3b. Moreover, the CE can still be maintained at >95% for 92 cycles and 56 cycles at the elevated current densities of 1 mA cm^{-2} and 2 mA cm^{-2}, respectively, as plotted in Fig. S8.† Even at a higher current density of 3 mA cm^{-2} with a capacity of 2 mA h cm^{-2}, the TD-COF@Cu cell was able to cycle for more than 40 cycles, while the bare copper cell shorted out in less than 2 cycles. The significant advancement in coulombic efficiency and postponement of electrode failure indicate that the TD-COF layer can suppress parasitic reactions and retain more available Li during the repeated cycles.
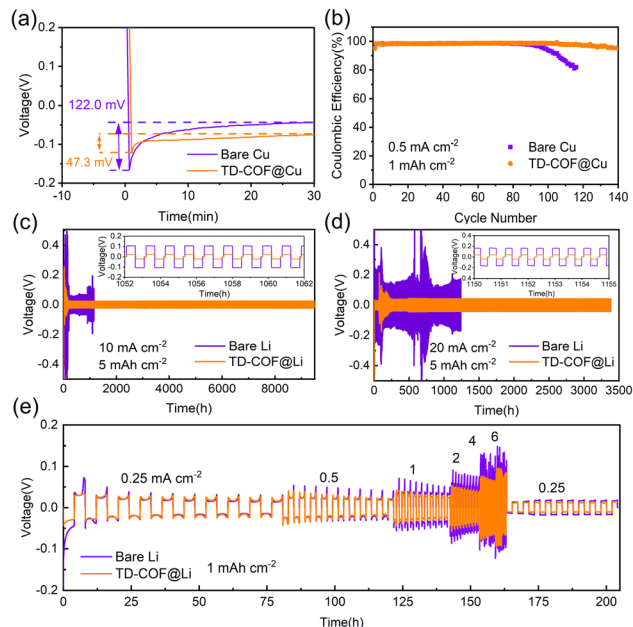
To further investigate the lifespan and operational feasibility of TD-COF on the reversibility of long-term charge–discharge cycles at different harsh current densities, a Li|Li symmetrical battery was assembled with TD-COF@Li and bare Li electrodes. The initial variable interface composition and prolonged process of methodical charge distribution make a profound contribution towards the voltage fluctuations. As shown in Fig. 3c, d and S9,† it is noteworthy that the electrochemical performance of Li|Li symmetric batteries modified with TD-COF is significantly improved compared with that of the bare Li batteries. The large fluctuant overpotential and greatly curtailed lifespan of bare Li based cells confirm the continuous interphase deterioration. In sharp contrast, the TD-COF@Li based cells achieved extraordinary constant voltage fluctuations of 35.1 mV, 46.7 mV and 80.7 mV and significantly enhanced lifetimes of 7400 hours, 9400 hours and 3300 hours at current densities of 5 mA cm^{-2}, 10 mA cm^{-2} and 20 mA cm^{-2}, respectively, which surpass the previously reported results for 2D COF artificial coating layers (Table S2†). In addition, the TD-COF@Li electrode exhibits preeminent rate performance with a smaller voltage hysteresis at various current densities ranging from 0.25 to 6 mA cm^{-2} (Fig. 3e), which reflects the ability of TD-COF to accelerate fast Li$^+$ migration.

Cycle-dependent electrochemical impedance spectroscopy (EIS) was used to investigate the evolution of the interface, as shown in Fig. S10 and Table S3.† The slightly increased resistance during the initial cycles can be reasonably attributed to poor electronic conductivity due to the semiconducting nature

of the pristine TD-COF layer and the sustainable rearrangement of Li ion transport channels adjacent to the TD-COF|Li interface. Notably, with the enriched SEI generation on TD-COF@Li, the gradual decrease in interfacial and charge transfer resistances indicate increased ionic conductivity after 50 cycles, which is consistent with the variational tendency of Li|Li symmetrical batteries. Moreover, the higher Li^+ transfer number of 0.78 in Fig. S12 and Table S4† further reinforces the conclusion that TD-COF can modulate mass Li^+ flux transfer with lower concentration polarization through the rigid 3D pathway and stabilize the interphase. On this basis, it can be re-emphasized that the TD-COF layer endowed with strong electron-rich sites confers rapid translocation of Li^+ with decreased interface resistance by virtue of the derived passivated SEI film.

At the same time, the potential Li^+ migration paths and corresponding migration energy barriers for the 3D configuration were further optimized and analysed to reveal the structure-dominated electrochemical performance. In sharp contrast to the ordered, vertically aligned 1D channels in a classical layered COF, wraparound anticlockwise and clockwise ion migration behaviors were conceived for TD-COF, as shown in Fig. 4, S13 and S14.† Specifically, the Li^+ ions transfer along the surrounded one-dimensional channel in an orthogonal direction according to either anticlockwise paths (paths 1–4) periodically migrating as $Li_1 \rightarrow Li_2 \rightarrow Li_3 \rightarrow Li_4 \rightarrow Li_5$ (Li_1) or clockwise paths (paths 5–8) in the manner of $Li_6 \rightarrow Li_7 \rightarrow Li_8 \rightarrow Li_9 \rightarrow Li_{10}$ (Li_6). The calculated migration energy barriers reveal measurably higher energy barriers in the anticlockwise paths, especially path 1 with a value of 1.78 eV in Fig. 4b and c, than that of clockwise path 5 with a maximum value of 0.92 eV. In addition to the spatially centrosymmetric matrix, another

straightforward insight into the difference between the migration barriers of the clockwise and anticlockwise paths is that it may caused by the different interactions of O atoms with Li^+. The migration distance of Li^+ in contact with O atoms in the anticlockwise path is longer than that in the clockwise path (Fig. S14†), thus the shorter distance in the clockwise path implies reduced interference from other atoms on the Li^+ migration.

In addition, the complexities of the interlayer migration (paths 9 and 10) and path transfer conversion (Path 11) in TD-COF were also evaluated, as shown in Fig. S15.† The higher interlayer migration energy barrier of an anticlockwise path is 1.04 eV (path 10, $Li_4 \rightarrow Li_{12}$), as opposed to 0.62 eV (path 9, $Li_{11} \rightarrow Li_7$) for a clockwise path, indicating that Li^+ is inclined to migrate through the clockwise interlayer cavity to another neighboring clockwise one-dimensional channel. The path transformation from clockwise to anticlockwise tends to be hindered due to the higher migration energy barrier of 1.17 eV (path 11, $Li_{11} \rightarrow Li_5$). In general, the TD-COF layer showcases a great ability to accelerate the charge transfer with a higher Li^+ transfer number of 0.78 (Fig. S12†), which can slow down the Li^+ concentration polarization via passing through the one-dimensional channel to interlayer cavity in sequential clockwise wraps.

To further reveal the inherent relationship between the improved electrochemical reversibility and the TD-COF artificial layer, the topographic textures of cycled Li metal were visually analyzed. The SEM images of the front and side views in Fig. S16† revealed that the TD-COF film was uniformly coated on the lithium metal surface with a thickness of about 8 μm. It is well-known that the Li volume variance during repeated charge and discharge processes is the main cause of infinite swelling and cracking of the SEI. As shown in Fig. 5, the modified electrode exhibited a tightly packed smooth morphology without the appearance of cracks and dendrites after plating and stripping protocols at the 300th cycle, which is conducive to minimizing the exposure area of fresh lithium in the electrolyte. After the corresponding cycling, significant gaps and moss-like lithium dendrites were observed from the bare Li counterpart, and the porous and rough surface undoubtedly exacerbated the loose Li accumulation and dead Li stacking because of the uneven distribution of the electric field. Due to the numerous faults and collapse, the substantial damage to the natural SEI with continuous electrolyte consumption of the bare Li electrode undoubtedly induced the available lithium decrement from a thickness of 497.4 μm to 363.5 μm, in sharp contrast with that of 505.2 μm to 460.4 μm for TD-COF@Li shown in Fig. 5c and f. In addition, in situ optical microscopy images exhibit that the bare Li electrode shows sudden growth of Li protrusions after the initial 10 min deposition (Fig. S17†), while the TD-COF-modified lithium remains relative smooth (Fig. 5j–l). These major improvements indicate that the unique spatial structure and numerous lithium affinity sites of TD-COF not only provide unimpeded charge transfer channels but also homogeneous nucleation sites. The inhibited spread of lithium dendrites and reformed electrochemical interphase stability are
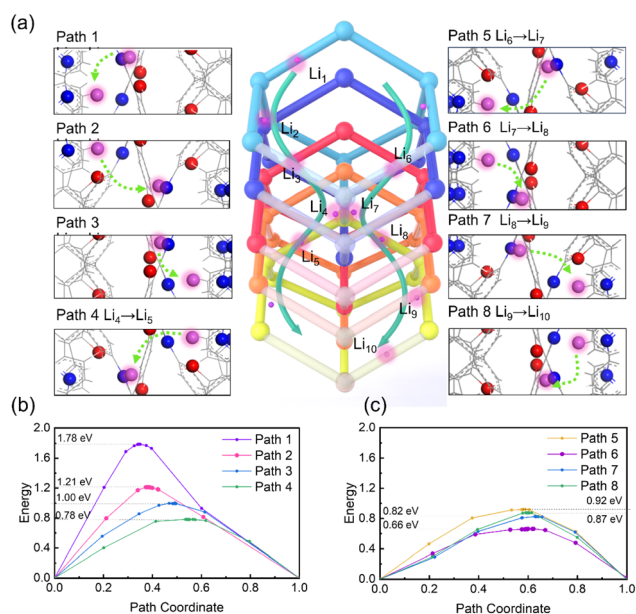

Fig. 4 Schematic illustrations of the suggested Li^+ migration pathways in TD-COF (a), and the corresponding energy barriers for anticlockwise (b) and clockwise (c) path migration.
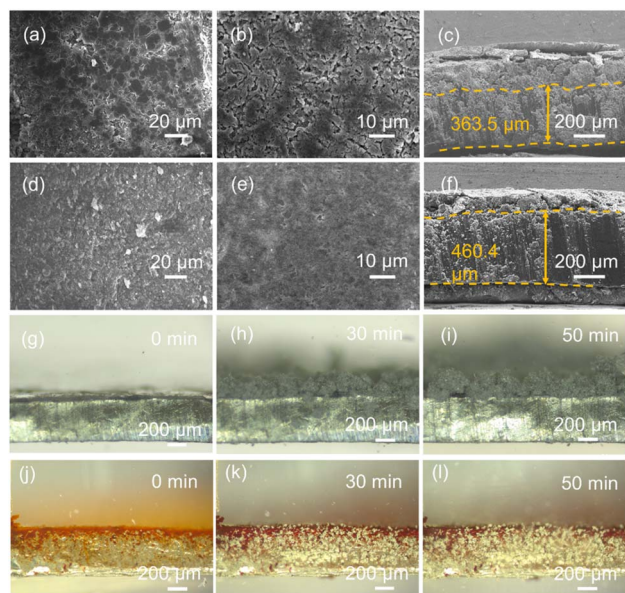
Fig. 5 Surface morphology characterizations of bare Li (a–c) and TD-COF@Li (d–f) electrodes in Li|Li symmetric batteries after 300 cycles at 4 mA cm^{-2} and 2 mA h cm^{-2}. Lithium plating (a, c and d, f), lithium stripping (b and e). *In situ* optical microscopy observation of the Li deposition process on bare Li (g–i) and TD-COF@Li (j–l) at a current density of 5 mA cm^{-2} for 50 min.

in accordance with the important reversibility of Li|Cu and Li|Li batteries.

X-ray photoelectron spectroscopy (XPS) was carried out for a careful understanding of the variations in interfacial composition. As shown in Fig. 6, both electrodes were mainly composed of a mixture of organic ($-O-C=O$, $C-O-C$, $ROCO_2Li$) and inorganic (Li_2CO_3, Li_3N, Li_xSO_y) species.[59] The organic substances of $ROCO_2Li$ (53.7 eV), RCO_2Li (54.3 eV), $-O-C=O$

(287.8 eV), $C-O-C$ (284.9 eV), and $C-C$ (283.8 eV) fitted from Li 1s and C 1s spectra have been identified as products from the decomposition of the ether-based solvent at low voltage during SEI formation.[60,61] Typically, the peak intensities of N 1s-, F 1s-, and S 2p-associated inorganic and organic compounds of Li_3N, $Li_2SO_2CF_3$, $Li_2NSO_2CF_3$, LiF and Li_xSO_y derived from NO_3^- and $TFSI^-$ anions in the TD-COF@Li sample are remarkably decreased with respect to those of the bare Li anode,[62] which strongly demonstrates that the TD-COF layer can effectively inhibit the reaction between LiTFSI and Li metal. In addition, the higher relative percentage of LiF in the TD-COF-modulated SEI layer indicates the nature of the superior interfacial Li$^+$ transfer kinetics.[63] This stable SEI configuration avoids Li dendrites and energy-barrier-reduced interfacial chemistry to considerably extend battery lifespan.

The reliable durability of TD-COF@Li in practical implementation was tested by pairing sulfur (S) and lithium iron phosphate (LFP) cathodes, and the results are shown in Fig. 7 and S18.† The voltage hysteresis values of 436.0, 334.7 and 323.2 mV for bare Li, and 488.9, 313.0 and 310.3 mV for TD-COF@Li-based Li|S full cells corresponding to 5, 100, and 200 cycles are depicted in Fig. 7a and b. After the interfacial activation at the initial 5 cycles, the subsequent measurable decreased voltage overpotentials indicate that the TD-COF layer endowed with enriched LiF indeed facilitates the rapid Li$^+$ transfer passing through the 3D spatial channels, which is consistent with half-cell cycling and EIS results. The long-term cycling performance of the Li|S full cell was also tested at a current density of 1C, as shown in Fig. 7c. The TD-COF@Li-based battery has a higher reversible capacity of 406.49 mA h g^{-1} after 500 cycles, which exceeds that of the bare Li|S battery of 336.56 mA h g^{-1}. In addition, the rate performance of the TD-COF@Li-based full battery also shows a significant capacity gap compared to the bare Li|S battery (as shown in Fig. 7d). Similarly, the LFP full cells with a TD-COF artificial SEI layer also exhibited superior performance properties including a lower voltage hysteresis, higher charge-transport efficiency and enhanced fast charging/ discharging ability, which are preferable to the bare-Li-based
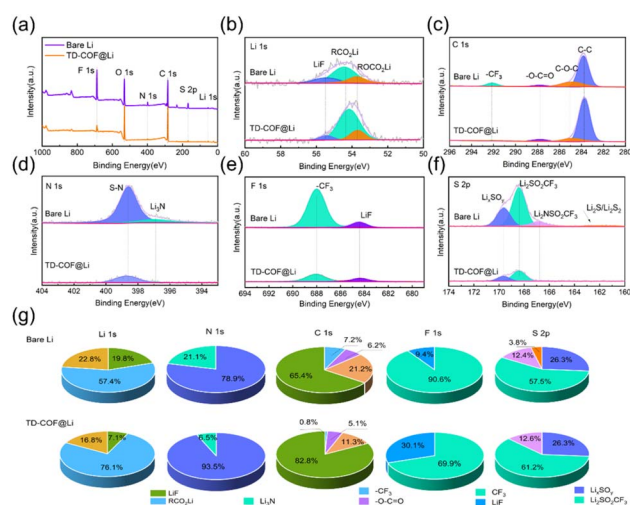

Fig. 6 XPS spectra of Li 1s, C 1s, N 1s, F 1s and S 2p for bare Li and TD-COF@Li electrodes (a–f) and the corresponding contents percentage of different chemicals (g) in Li|Li symmetric batteries after 300 cycles at 4 mA cm^{-2} and 2 mA h cm^{-2}.
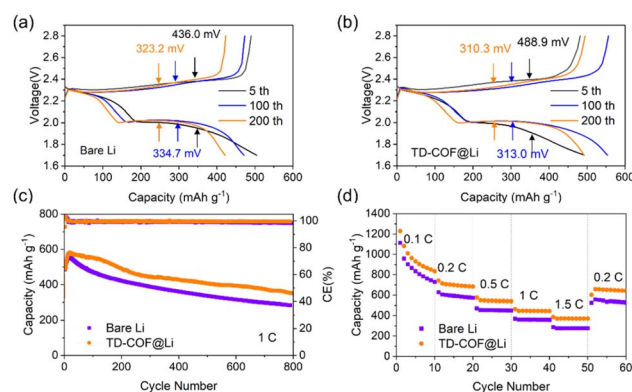

Fig. 7 Electrochemical performance of the Li|S full cell assembled with bare Li and TD-COF@Li electrodes. The galvanostatic charge/ discharge curves (a and b), long-term cycling (c) and rate performance (d) when operated at different current densities.

counterpart. The enhancement effect of the TD-COF-modified Li|LFP full cell is consistent with that of the Li|S full cell. Overall, a reasonable conclusion that can be made based on these gratifying achievements in maintaining a low interfacial resistance, slight polarization, and considerable capacity retention is that the efficient TD-COF artificial SEI plays an indispensable role in the stabilization of LMBs.

Conclusions

In conclusion, the highly crystalline 3D TD-COF with a *dia-c7* topology was successfully synthesized and exploited as an artificial SEI layer to regulate and strengthen the lithium interfacial stability. The unfolding three-dimensional space with interpenetrated building blocks anchoring a substantial number of lithiophilic sites of $-C{=}N-$ and $-OH$ offers compelling benefits for speeding up the migration of Li^+ flux ($t_{Li^+} = 0.78$) in a clockwise pathway. The methodized charge distribution with lower energy barriers makes a profound contribution towards Li^+ desolvation and dendrite-free Li deposition. The derived LiF-rich SEI layer enables the formation of thin and homogeneous interphases to consolidate and extend the modified electrode lifespan. Compared with pristine Li, the TD-COF@Li electrode demonstrates intriguing properties of superior Li^+ utilization, a lower nucleation barrier and prolonged reversibility in Li|Cu, Li|Li, Li|S and Li|LFP full batteries. This viable guidance emphasizes that profound attention should be paid towards the further development of innovative 3D COF polymer-modified layers that are capable of realizing high-performance Li metal batteries.

Data availability

The data that support the findings of this study are available from the corresponding author upon reasonable request.

Author contributions

K. Y. Z. and Y. T. Z. conceived and designed the experiments. K. Y. Z., Z. Y. G., C. Z., Y. Q. Z., and Y. H. Z. performed the experiments. K. Y. Z. and Y. Y. D. conducted structural simulations and DFT calculations. K. Y. Z. and Y. T. Z. wrote and revised the manuscript. Y. T. Z. and S. J. L. directed the research.

Conflicts of interest

There are no conflicts to declare.

Acknowledgements

Notes and references

1 Z. A. Ghazi, Z. Sun, C. Sun, F. Qi, B. An, F. Li and H. M. Cheng, *Small*, 2019, **15**, e1900687.

2 J. Ma, Y. Li, N. S. Grundish, J. B. Goodenough, Y. Chen, L. Guo, Z. Peng, X. Qi, F. Yang, L. Qie, C.-A. Wang, B. Huang, Z. Huang, L. Chen, D. Su, G. Wang, X. Peng, Z. Chen, J. Yang, S. He, X. Zhang, H. Yu, C. Fu, M. Jiang, W. Deng, C.-F. Sun, Q. Pan, Y. Tang, X. Li, X. Ji, F. Wan, Z. Niu, F. Lian, C. Wang, G. G. Wallace, M. Fan, Q. Meng, S. Xin, Y.-G. Guo and L.-J. Wan, *J. Phys. D: Appl. Phys.*, 2021, **54**, 183001.

3 H. Li, *Joule*, 2019, **3**, 911–914.

4 W. Cao, J. Zhang and H. Li, *Energy Storage Mater.*, 2020, **26**, 46–55.

5 Y.-F. Meng, H.-J. Liang, C.-D. Zhao, W.-H. Li, Z.-Y. Gu, M.-X. Yu, B. Zhao, X.-K. Hou and X.-L. Wu, *J. Energy Chem.*, 2022, **64**, 166–171.

6 Y. Chen, J. Xu, P. He, Y. Qiao, S. Guo, H. Yang and H. Zhou, *Sci. Bull.*, 2022, **67**, 2449–2486.

7 D. Meggiolaro, M. Agostini and S. Brutti, *ACS Energy Lett.*, 2023, **8**, 1300–1312.

8 Z.-X. Huang, X.-L. Zhang, X.-X. Zhao, H.-Y. Lü, X.-Y. Zhang, Y.-L. Heng, H. Geng and X.-L. Wu, *J. Mater. Sci. Technol.*, 2023, **160**, 9–17.

9 C.-D. Zhao, J.-Z. Guo, Z.-Y. Gu, X.-T. Wang, X.-X. Zhao, W.-H. Li, H.-Y. Yu and X.-L. Wu, *Nano Res.*, 2022, **15**, 925–932.

10 J. Huang, Z. Huang, X. Zheng, Y. Wang, X. Rui, Y. Yu, S.-X. Dou and C. Wu, *Energy Storage Mater.*, 2024, **70**, 103420.

11 J. Huang, K. Wu, G. Xu, M. Wu, S. Dou and C. Wu, *Chem. Soc. Rev.*, 2023, **52**, 4933–4995.

12 Q. Zhang and Y.-G. Guo, *Acta Phys.-Chim. Sin.*, 2020, **37**, 2011061.

13 D. Lin, Y. Liu and Y. Cui, *Nat. Nanotechnol.*, 2017, **12**, 194–206.

14 F. Hao, A. Verma and P. P. Mukherjee, *J. Mater. Chem. A*, 2018, **6**, 19664–19671.

15 B. Li, Y. Chao, M. Li, Y. Xiao, R. Li, K. Yang, X. Cui, G. Xu, L. Li, C. Yang, Y. Yu, D. P. Wilkinson and J. Zhang, *Electrochem. Energy Rev.*, 2023, **6**, 7.

16 X. B. Cheng, R. Zhang, C. Z. Zhao, F. Wei, J. G. Zhang and Q. Zhang, *Adv. Sci.*, 2016, **3**, 1500213.

17 X. He, D. Bresser, S. Passerini, F. Baakes, U. Krewer, J. Lopez, C. T. Mallia, Y. Shao-Horn, I. Cekic-Laskovic, S. Wiemers-Meyer, F. A. Soto, V. Ponce, J. M. Seminario, P. B. Balbuena, H. Jia, W. Xu, Y. Xu, C. Wang, B. Horstmann, R. Amine, C.-C. Su, J. Shi, K. Amine, M. Winter, A. Latz and R. Kostecki, *Nat. Rev. Mater.*, 2021, **6**, 1036–1052.

18 Y. Han, B. Liu, Z. Xiao, W. Zhang, X. Wang, G. Pan, Y. Xia, X. Xia and J. Tu, *InfoMat*, 2021, **3**, 155–174.

19 Y. Liao, L. Yuan, X. Liu, J. Meng, W. Zhang, Z. Li and Y. Huang, *Energy Storage Mater.*, 2022, **48**, 366–374.

20 J. Xiao, Q. Li, Y. Bi, M. Cai, B. Dunn, T. Glossmann, J. Liu, T. Osaka, R. Sugiura, B. Wu, J. Yang, J.-G. Zhang and M. S. Whittingham, *Nat. Energy*, 2020, **5**, 561–568.

21 Q. Wang, T. Lu, Y. Liu, J. Dai, L. Guan, L. Hou, H. Du, H. Wei, X. Liu, X. Han, Z. Ye, D. Zhang, Y. Wei and H. Zhou, *Energy Storage Mater.*, 2023, **55**, 782–807.

22 G. M. Hobold, J. Lopez, R. Guo, N. Minafra, A. Banerjee, Y. Shirley Meng, Y. Shao-Horn and B. M. Gallant, *Nat. Energy*, 2021, **6**, 951–960.

23 Y. Wu, F. Ma, Z. Zhang, D. Chen, H. Yu, X. Zhang, F. Ding, L. Zhang and Y. Chen, *EcoEnergy*, 2024, **2**, 299–310.

24 C. Wei, Z. Yao, J. Ruan, Z. Song, A. Zhou, Y. Song, D. Wang, J. Jiang, X. Wang and J. Li, *Chin. Chem. Lett.*, 2024, **35**, 109330.

25 Y. Cheng, B. Liu, X. Li, X. He, Z. Sun, W. Zhang, Z. Gao, L. Zhang, X. Chen, Z. Chen, Z. Chen, L. Peng and X. Duan, *Carbon Energy*, 2024, e599.

26 H.-Y. Li, C. Li, Y.-Y. Wang, W.-D. Dong, X.-K. Zhang, M.-H. Sun, Y. Li and B.-L. Su, *Chem. Synth.*, 2023, **3**, 30.

27 J. Jiang, M. Li, X. Liu, J. Yi, Y. Jiang, C. Wu, H. Liu, B. Zhao, W. Li, X. Sun, J. Zhang and S. Dou, *Adv. Energy Mater.*, 2024, **14**, 2400365.

28 S. Gao, F. Sun, N. Liu, H. Yang and P.-F. Cao, *Mater. Today*, 2020, **40**, 140–159.

29 T. Jin, J. S. Chen, X. C. Chen, N. W. Li and L. Yu, *Next Energy*, 2023, **1**, 100040.

30 Q. Li, H. Liu, F. Wu, L. Li, Y. Ye and R. Chen, *Angew. Chem., Int. Ed.*, 2024, **63**, e202404554.

31 R. K. Petla, I. Lindsey, J. Li and X. Meng, *ChemSusChem*, 2024, **17**, e202400281.

32 R. Zhang, N.-W. Li, X.-B. Cheng, Y.-X. Yin, Q. Zhang and Y.-G. Guo, *Adv. Sci.*, 2017, **4**, 1600445.

33 S. Gao, Z. Li, N. Liu, G. Liu, H. Yang and P. F. Cao, *Adv. Funct. Mater.*, 2022, **32**, 2202013.

34 W. Wang, Z. Yang, Y. Zhang, A. Wang, Y. Zhang, L. Chen, Q. Li and S. Qiao, *Energy Storage Mater.*, 2022, **46**, 374–383.

35 Y. Zhang, W. Wang, M. Hou, Y. Zhang, Y. Dou, Z. Yang, X. Xu, H. Liu and S. Qiao, *Energy Storage Mater.*, 2022, **47**, 376–385.

36 J. You, H. Deng, X. Zheng, H. Yan, L. Deng, Y. Zhou, J. Li, M. Chen, Q. Wu, P. Zhang, H. Sun and J. Xu, *ACS Appl. Mater. Interfaces*, 2022, **14**, 5298–5307.

37 L. Wang, L. Zhang, Q. Wang, W. Li, B. Wu, W. Jia, Y. Wang, J. Li and H. Li, *Energy Storage Mater.*, 2018, **10**, 16–23.

38 L. Chen, J. G. Connell, A. Nie, Z. Huang, K. R. Zavadil, K. C. Klavetter, Y. Yuan, S. Sharifi-Asl, R. Shahbazian-Yassar, J. A. Libera, A. U. Mane and J. W. Elam, *J. Mater. Chem. A*, 2017, **5**, 12297–12309.

39 S. Ni, M. Zhang, C. Li, R. Gao, J. Sheng, X. Wu and G. Zhou, *Adv. Mater.*, 2023, **35**, 2209028.

40 J. Yang, T. Feng, J. Hou, X. Li, B. Chen, C. Chen, Z. Chen, Y. Song and M. Wu, *J. Energy Chem.*, 2022, **65**, 583–591.

41 B. Zhang, Z. Ju, Q. Xie, J. Luo, L. Du, C. Zhang and X. Tao, *Energy Storage Mater.*, 2023, **58**, 322–331.

42 S. Wang, L. Zhou, M. K. Tufail, L. Yang, P. Zhai, R. Chen and W. Yang, *Chem. Eng. J.*, 2021, **415**, 128846.

43 Q. Wang, J. Yang, X. Huang, Z. Zhai, J. Tang, J. You, C. Shi, W. Li, P. Dai, W. Zheng, L. Huang and S. Sun, *Adv. Energy Mater.*, 2022, **12**, 2103972.

44 S. Li, J. Huang, Y. Cui, S. Liu, Z. Chen, W. Huang, C. Li, R. Liu, R. Fu and D. Wu, *Nat. Nanotechnol.*, 2022, **17**, 613–621.

45 Z. Zhao, Y. Zhang, Y. Dou, X. Li, X. Fan, Q. Li, H. Liu, Z. Xu, B. Zhang and X. Guo, *J. Membr. Sci.*, 2024, **705**, 122885.

46 M. Zhang, R. Tan, M. Wang, Z. Zhang, C. John Low and Y. Lai, *Battery Energy*, 2024, **3**, 20230050.

47 C. S. Diercks and O. M. Yaghi, *Science*, 2017, **355**, eaal1585.

48 X. Li, S. Cai, B. Sun, C. Yang, J. Zhang and Y. Liu, *Matter*, 2020, **3**, 1507–1540.

49 A. P. Cote, A. I. Benin, N. W. Ockwig, M. O'Keeffe, A. J. Matzger and O. M. Yaghi, *Science*, 2005, **310**, 1166–1170.

50 D. Chen, P. Liu, L. Zhong, S. Wang, M. Xiao, D. Han, S. Huang and Y. Meng, *Small*, 2021, **17**, 2101496.

51 Y. Yang, C. Zhang, G. Zhao, Q. An, Z. y. Mei, Y. Sun, Q. Xu, X. Wang and H. Guo, *Adv. Energy Mater.*, 2023, **13**, 2300725.

52 W. Wang, Y. Zhang, H. Jiang, R. Zhang, N. Wang, Y. Dou, Z. Zhao, X. Yang, X. Fan, X. Li, X. Guo, Q. Feng and S. Qiao, *Chem. Eng. J.*, 2023, **472**, 144888.

53 Y. Xiao, Y. Ling, K. Wang, S. Ren, Y. Ma and L. Li, *J. Am. Chem. Soc.*, 2023, **145**, 13537–13541.

54 B. Gui, G. Lin, H. Ding, C. Gao, A. Mal and C. Wang, *Acc. Chem. Res.*, 2020, **53**, 2225–2234.

55 H. M. El-Kaderi, J. R. Hunt, J. L. Mendoza-Cortés, A. P. Côté, R. E. Taylor, M. O'Keeffe and O. M. Yaghi, *Science*, 2007, **316**, 268–272.

56 X. J. Chen, C. R. Zhang, X. Liu, J. X. Qi, W. Jiang, S. M. Yi, C. P. Niu, Y. J. Cai, R. P. Liang and J. D. Qiu, *J. Hazard. Mater.*, 2023, **445**, 130442.

57 Z. Li, X. Ding, Y. Feng, W. Feng and B.-H. Han, *Macromolecules*, 2019, **52**, 1257–1265.

58 L. Shi, V. S. Kale, Z. Tian, X. Xu, Y. Lei, S. Kandambeth, Y. Wang, P. T. Parvatkar, O. Shekhah, M. Eddaoudi and H. N. Alshareef, *Adv. Funct. Mater.*, 2023, **33**, 2212891.

59 Q. Wu, Y. Zheng, X. Guan, J. Xu, F. Cao and C. Li, *Adv. Funct. Mater.*, 2021, **31**, 2101034.

60 F. Qiu, X. Li, H. Deng, D. Wang, X. Mu, P. He and H. Zhou, *Adv. Energy Mater.*, 2019, **9**, 1803372.

61 X. Ren, P. Gao, L. Zou, S. Jiao, X. Cao, X. Zhang, H. Jia, M. H. Engelhard, B. E. Matthews, H. Wu, H. Lee, C. Niu, C. Wang, B. W. Arey, J. Xiao, J. Liu, J.-G. Zhang and W. Xu, *Proc. Natl. Acad. Sci. U. S. A.*, 2020, **117**, 28603–28613.

62 Y. Zhang, Z. Gou, K. Zheng, Y. Dou and Z. Zhou, *J. Phys. Chem. Lett.*, 2024, **15**, 6598–6604.

63 Z. Wang, F. Qi, L. Yin, Y. Shi, C. Sun, B. An, H. M. Cheng and F. Li, *Adv. Energy Mater.*, 2020, **10**, 1903843.